

Strain-enabled ultra-broadband Ge-based photonic devices for low-cost integration in PICs

Yiding Lin (✉ liny0075@e.ntu.edu.sg)

Nanyang Technological University <https://orcid.org/0000-0002-9854-2072>

Danhao Ma

Massachusetts Institute of Technology

Rui-Tao Wen

Southern University of Science and Technology

Kwang Hong Lee

Singapore-MIT Alliance for Research and Technology (SMART)

Govindo Syaranamual

Singapore-MIT Alliance for Research and Technology

Lionel Kimerling

Massachusetts Institute of Technology

Chuan Seng Tan

Nanyang Technological University

Jurgen Michel

Massachusetts Institute of Technology

Article

Keywords: Photonic-integrated circuits, global data communication, cost-effective, ultra-broadband

Posted Date: August 24th, 2020

DOI: <https://doi.org/10.21203/rs.3.rs-60601/v1>

License:  This work is licensed under a Creative Commons Attribution 4.0 International License.

[Read Full License](#)

Abstract

Photonic-integrated circuits (PICs) have become one of the most promising solutions to the burgeoning global data communication and are being envisioned to have revolutionary impact in many other emerging fields. This outlook requires future PICs to be significantly more broadband and cost-effective. The current germanium (Ge)-based active photonic devices in PICs are thus facing a new bandwidth-cost trade-off. Here, we demonstrate ultra-broadband, high-efficiency Ge photodetectors up to 1,630 nm operation wavelength and $\text{Ge}_{0.99}\text{Si}_{0.01}$ electro-absorption (EA) modulator arrays with an operating range of ~ 100 nm from 1,525 to 1,620 nm, using a CMOS-compatible recess-type silicon nitride (SiN_x) stressor. The broadband operation could facilitate a wide (>100 nm) window for low-cost Ge modulator-detector co-integration, requiring only a single step of Ge epitaxy and two different SiN_x depositions. The broad modulation and co-integration coverage can be entirely shifted to shorter ($\sim 1,300$ nm) and longer ($>1,700$ nm) wavelengths with small amounts of Si or tin (Sn) alloying. This proof-of-concept work provides a pathway for PICs towards future low-cost and high-data-capacity communication networks, immediately accessible by designers through foundries.

Introduction

The demand for high-speed and large-capacity data communication has surged in the past decade, primarily due to the advent of insatiable needs in the emerging fields of high-definition video streaming, cloud computing, internet-of-things, augmented reality, and many other applications. Photonic-integrated circuits (PICs) have thus been becoming one of the most promising solutions to potentially alleviate the speed, power, and bandwidth bottlenecks of its electronic counterparts at short-reach level interconnects (i.e. rack-to-rack, board-to-board, chip-to-chip and intra-chip) for high-performance computing and data center networks, by leveraging the state-of-the-art fiber-optic communication infrastructure and silicon (Si) CMOS technology^{1,2}. Beyond optical interconnects, PICs have recently been envisioned to have revolutionary impact on future sensing^{3,4}, quantum computing^{5,6,7}, artificial intelligence^{8,9,10}, and neuroscience^{11,12}, to name a few. The burgeoning global data demand and future widespread utilization require future PICs to be more broadband and cost-effective. For the common optical transceiver PICs, a straightforward solution to the broadband operation is to utilize the short-reach nature of the data center networks. Unlike conventional long-haul fiber-optic tele-communication, the fiber link length is much shorter (in the range of meters or below) among PIC-incorporated optical modules in data centers. The shorter length leaves a broader wavelength window and consequently higher capacity potential for low-loss transmission (e.g. intrinsic loss <0.4 dB/km from $\sim 1,300$ to $1,700$ nm¹³), using the commonly-adopted wavelength-division multiplexing (WDM) scheme. One may exploit this wider window for future broadband PICs; however, this would give rise to new challenges for the development of existing photonic devices in PICs. For example, Ge, due to its CMOS-compatibility, considerable absorption coefficient¹⁴, and significant Franz-Keldysh effect¹⁵ around 1,550 nm, has become an indispensable material in PICs for high-performance photodetectors^{16,17,18,19,20} and electro-absorption (EA) modulators^{21,22,23,24,25,26}. With years of development, Ge has shown an optimal adaptability to foundry processes. As of now, Ge

photodetectors are ubiquitous in the process design kits (PDKs) of most silicon photonics foundries, and Ge EA modulators are also being actively included. Compared to the Si counterparts, Ge EA modulators have exhibited a smaller device footprint and lower power consumption than Mach-Zehnder modulators^{27, 28}, as well as a wider operating spectrum and superior temperature insensitivity than microring (MR) modulators^{29, 30}. Furthermore, MR modulators need additional control electronics and consequently increased power consumption to stay on resonance. However, the operating spectra of both devices remain limited compared to the potential low-loss window. The quantum efficiency of Ge photodetectors drastically drops beyond the *C*-band ($>\sim 1,570$ nm); while Ge EA modulators generally exhibit a narrow optical bandwidth of 30 nm ($\sim 1,610$ – $1,640$ nm) depending on the applied bias and insertion loss. Although GeSn³¹ epitaxy and separate steps of GeSi epitaxy with different Si compositions can be viable for broadband photo-detection and EA modulation, it would inevitably lead to process complexity with increased cost. Likewise, heterogeneous integration via die bonding³² or transfer printing³³ demands multiple bandgap-varied materials and stringent yield control. Another side effect from the bandwidth limitation is the operating spectra incompatibility between the Ge photodetectors and EA modulators. As discussed, Ge photodetectors display an optimal performance up to the *C*-band; whereas Ge EA modulators work most efficiently in the *L*-band ($\sim 1,610$ nm). This poses a challenge to integrate both devices into a single transceiver PIC to fully harness their individual performance potential. Similar drawbacks of process complexity and integration cost would remain if multiple epitaxial steps are employed. Therefore, enabling a broadband operation and co-integration of Ge-based photodetectors and EA modulators in a single epitaxial growth is of paramount importance for future high-capacity and low-cost PICs.

Prior studies have adopted a single epitaxy step for platforms that are potentially suitable for the modulator-detector co-integration and their broadband operation. Chaisakul *et al.*³⁴ realized a Ge/SiGe multi-quantum-well (MQW)-based platform in a single epitaxy step and demonstrated a Ge optical interconnect with co-integrated photodetectors and EA modulators. However, the epi-layer stack is too thick (~ 10 μm) for practical front-end-of-line integration and the resulting link optical bandwidth remains limited (~ 20 nm). Additionally, the Si-incorporated MQW design makes the platform difficult for a broader operating wavelength coverage. Furthermore, Littlejohns *et al.*³⁵ employed a single step of GeSi rapid melting growth on a tree-like structure and realized a GeSi strip array with varied inter-strip but uniform intra-strip Ge compositions. However, this technique lacks further device demonstration.

Here, we demonstrate an approach of utilizing a recess-type silicon nitride (SiN_x) stressor for Ge photodetectors and $\text{Ge}_{0.99}\text{Si}_{0.01}$ EA modulator arrays with ultra-broad optical bandwidths. The SiN_x stressor induces mechanical strain in the Ge-based materials for their bandgap tuning and the broadband device operation. The recessed stressor configuration at sidewalls prominently enhances both the strain magnitude and uniformity and leads to a wider operating optical bandwidth. As a proof of concept, recessed tensile (~ 600 MPa) SiN_x -strained waveguide-shaped Ge-on-insulator (*w*-Ge-OI) metal-semiconductor-metal (MSM) photodetectors exhibit an extension of the photocurrent roll-off by ~ 70 nm to 1,612 nm, with a $\sim 3.3\times$ enhancement on the absorption coefficient. The concept is easily transferrable

to conventional Ge photodetectors on-Si or -silicon-on-insulator (-SOI) wafers. The broadband EA modulation is achieved in device arrays utilizing the $\text{Ge}_{0.99}\text{Si}_{0.01}$ strain tunability dependent on the $\text{Ge}_{0.99}\text{Si}_{0.01}$ width with an identical SiN_x stressor. By varying the $\text{Ge}_{0.99}\text{Si}_{0.01}$ width from 0.4 to 4.0 μm with the similar 600-MPa tensile stressor, the operation of $\text{Ge}_{0.99}\text{Si}_{0.01}$ EA modulator arrays on-SOI spans from $\sim 1,525$ to $\sim 1,620$ nm, with an extinction-ratio-to-insertion-loss (ER/IL) ratio above 1.3 at a reverse bias of -6 V. Incorporating an additional separate compressive (~ 1 GPa) stressor could extend the total coverage from $\sim 1,460$ to $\sim 1,620$ nm. In addition, the wider operating coverages of both devices are expected to facilitate a broadband (>100 nm, $\sim 1,520$ – $1,630$ nm) Ge modulator-detector co-integration, by applying compressive (1 GPa) and tensile (600 MPa) stressors on the modulator arrays and photodetectors, respectively. Both, the broadband operations and the co-integration require only a single step of Ge-based growth and a maximum of two different SiN_x depositions, one tensile and the other compressive, enabling simple and low-cost integration. Furthermore, the Si composition can be increased to 4% to shift the entire broad operating range to $\sim 1,300$ nm, while Sn can also be alloyed into Ge for an operating coverage beyond 1,700 nm. The mature SiN_x -based process^{36,37} makes this approach readily accessible in the state-of-the-art foundries. Compared to other Ge strain engineering techniques^{38,39,40}, the recessed SiN_x stressor maintains both CMOS-compatibility and small device footprint for compact integration. Foreseeably, the operating bandwidth can be further extended by using a SiN_x stressor with higher stress. This technique provides a pathway for future broadband and low-cost PICs with co-integrated Ge-based EA modulator and photodetector arrays (Fig. 1) and can be potentially applied to other semiconductor material platforms (e.g. III-V, 2D) for bandgap engineering and corresponding diversified electronic and photonic applications.

Results And Discussion

Recessed SiN_x stressor for enhanced and uniform mechanical strain

To present a wider adaptability of this technique, as a proof of concept, the broadband photodetection and EA modulation were demonstrated on Ge-on-insulator (Ge-OI) and $\text{Ge}_{0.99}\text{Si}_{0.01}$ on SOI platforms, respectively. The Ge-OI photodetectors are first discussed. In contrast to the technical maturity of the Ge-on-SOI platform, the Ge-OI platform is recently gaining attention for both advanced electronic⁴¹ and photonic^{42,43,44} applications. In this work, the Ge-OI was formed on a 200-mm Si (100) wafer via Ge-on-Si epitaxy, bonding, and layer transfer, using silicon dioxide (SiO_2) as the intermediate insulator layer⁴⁵. The detailed fabrication process is discussed in Supplementary section S1. The bonding and layer transfer approach could facilitate a scalable Ge-OI fabrication to any wafer diameter and Ge thickness, with a superior Ge quality than that from the direct Ge-on-Si epitaxy⁴⁶. Its low process thermal budget (~ 300 °C) enables a back-end-of-line electronic-photonic integration. It is without doubt that both the photodetectors and modulators can be demonstrated interchangeably on the other platform. The Ge-OI platform was also used to study the effect of the recessed SiN_x stressor on its induced Ge mechanical strain (Fig. 2). A tensile stressor is placed in trenches at both sides of w -Ge-OI and in contact with Ge via

the waveguide sidewalls (Fig. 2a); while deeper trenches are created into the underlying SiO₂ as the recessed configuration to accommodate the stressor (Fig. 2b). The modelling was performed using a finite element method, with a detailed description in Supplementary section S2. The results are shown in Fig. 2c, d. It was found that the transverse tensile strain (ϵ) in Ge is enhanced with the use of the recessed SiN_x stressor, especially at the bottom portion of Ge closer to the buried SiO₂. The strain uniformity is thus improved simultaneously. This increased uniformity is due to the recessed stressor configuration that allows the tensile stress to be applied on both the sidewalls of SiO₂ and Ge to pull on both materials. The constraint to the sidewall stressor from the underlying SiO₂ and Si bulk is therefore alleviated, enabling a uniform Ge strain profile without selective substrate removal to form suspended Ge structures^{38, 39}, which facilitates a more foundry-compatible strained-Ge integration. The longitudinal strain in Ge ($\sim 0.17\%$) reveals a negligible change irrespective of the use of the SiN_x stressor (Supplementary Fig. S2). For a quantitative illustration, the vertical (from O to A) and transverse (both O and A to the Ge/SiN_x interface) values (in Fig. 2c, d) were extracted and plotted in Fig. 2e, f, respectively. It can be clearly seen that the ϵ is enhanced by $\sim 2\times$ near the Ge/SiO₂ interface along the points O and A, with the 1-GPa recessed tensile SiN_x stressor (Fig. 2e). Additionally, variations along both the transverse (x -) and vertical (z -) directions are significantly reduced with the use of the recessed SiN_x stressor, again indicating a more homogeneous strain distribution. Similar effects can be expected for Ge-on-SOI and other material platforms with the use of both tensile and compressive recessed stressors.

To experimentally demonstrate the effect of the recessed SiN_x stressor, strained w -Ge-OI structures similar to that in the model (Fig. 2c, d) were fabricated, with the detailed process depicted in Supplementary Fig. S5. The SiN_x was deposited in a Cello Aegis-20 plasma-enhanced chemical vapor deposition (PECVD) system. Optimizing the deposition parameters results in a tensile film stress of ~ 600 MPa. The details on the stress characterization and optimization are discussed in Supplementary section S4. The SiN_x on the top of w -Ge-OI was removed via a second electron-beam lithography (EBL) followed by reactive-ion etching (RIE), as it induces undesired compressive strain to the Ge underneath (Supplementary Fig. S8). Chemical mechanical polishing (CMP) can be an alternative process for the top SiN_x removal at wafer scale. Cross-sectional scanning electron microscope (SEM) images of the fabricated structures are shown in Supplementary Fig. S6. The induced strain in Ge was characterized via commercial micro-Raman spectrometers at the longitudinal optical (LO) mode. More information about the measurement tools and calibration can be found in Methods. Two laser excitation wavelengths of 532 and 785 nm were used and lead to distinct photon penetration depths of ~ 9 and ~ 89 nm⁴⁷, respectively, into Ge, facilitating Raman spectra revealing depth-dependent strain information. For this reason, the w -Ge was thinned down to ~ 100 nm, allowing a full Ge thickness coverage for the strain acquisition at the laser excitation of 785 nm.

The micro-Raman spectra on 0.5 μm -wide w -Ge-OIs are shown in Fig. 2h. The laser spot diameter of ~ 1 μm at both 532 and 785 nm ensures a complete transverse coverage of the waveguide structures. It can be observed that the peak LO phonon frequencies of all spectra are red-shifted compared to that of bulk

Ge ($\sim 300.8 \text{ cm}^{-1}$), indicating that a tensile strain is induced in Ge as expected. It is important to mention that the widths of the w -Ge-OI sidewall trenches are within $10 \text{ }\mu\text{m}$ to accommodate the SiN_x stressor, and the corresponding Raman spectra exhibit a consistent Ge tensile strain independent of the trench width (Supplementary Fig. S10). The narrow trench width with a significant strain effect could envision a compact device integration. The Raman spectra reasonably overlap at both 532 and 785 nm for w -Ge-OIs with the recessed stressor, while only a partial overlap below $\sim 300 \text{ cm}^{-1}$ was seen for that with the non-recessed stressor. The broader full-width-at-half-maximum (FWHM, $\sim 12.90 \text{ cm}^{-1}$) of the spectrum for the non-recessed w -Ge-OI at 785 nm, compared to the recessed structure ($\sim 9.04 \text{ cm}^{-1}$), is attributed to the strain non-uniformity rather than strain-induced crystal quality deterioration⁴⁸. This conclusion is made based on the gradual blue shift of the peak LO phonon frequencies with time, observed from some early-batch tensile-strained w -Ge-OIs (Supplementary Fig. S9), where the SEM inspection reveals delaminated stressors from the w -Ge-OI sidewalls. The matching Raman spectra with respect to an un-strained w -Ge-OI ($\sim 300 \text{ cm}^{-1}$), after the stressor delamination, verify that the stressor has not caused any Ge crystal quality degradation. Therefore, the phenomena in Fig. 2h suggests an improved strain uniformity in Ge vertically along the z -axis as seen in Fig. 2d. Furthermore, it can be inferred that the Ge is compressively strained at the bottom part of Ge closer to the Ge/ SiO_2 interface, since the deeper-penetrating Raman spectrum at 785 nm (Fig. 2h, upper panel) exhibits a shoulder at $\sim 305 \text{ cm}^{-1}$ while the spectrum at 532 nm does not. The compressive strain might be due to both the substrate constraint from the SiO_2 -on-Si bulk and the tensile strain at the top portion of w -Ge, which collectively exerts a compressing force to the bottom part of w -Ge. The reason for no compressive strain shown in the finite element simulation pertains probably to the thinner substrate thickness ($100 \text{ }\mu\text{m}$) employed in the simulation than a 200-mm Si wafer ($\sim 725 \text{ }\mu\text{m}$), which alleviates the substrate constraint. The compressive Raman shoulder was suppressed with the adoption of the recessed stressor (Fig. 2h, lower panel), suggesting a strain enhancement at the bottom part of Ge. This agrees well with the mechanism of the recessed stressor from the simulation (Fig. 2c, d). As the tensile stressor at both sidewalls essentially pulls the sandwiched Ge in the middle for a tensile strain, the adhesion of the stressor to the sidewalls becomes critical. It is noteworthy that oxygen (O_2) plasma treatment significantly enhances the duration of the stressor adhesion (Supplementary Fig. S9). Additional micro-Raman measurements on $2 \text{ }\mu\text{m}$ -wide w -Ge-OIs find that the compressive strain is accumulated close to sidewalls at the bottom part of w -Ge-OI, which was turned into tensile strain with the use of the recessed stressor (Supplementary Fig. S7), thus improving the Ge strain uniformity with an enhanced magnitude. The mechanism can be similarly applied to the recessed compressive SiN_x stressor for the magnitude and uniformity enhancement of the compressive strain.

Broadband strained Ge-OI MSM photodetectors

To investigate the effect of the recessed SiN_x stressor on the performance of Ge photo-detection, metal-semiconductor-metal (MSM) photodetectors were developed based on the strained w -Ge-OI structures, with a schematic shown in Fig. 3a. As a reference, MSM detectors on w -Ge-OIs without stressor were also

fabricated. All w -Ge-OIs have identical Ge width of 1 μm and thickness of 400 nm. The detailed fabrication for all the devices is illustrated in Supplementary section S8. It is noteworthy that Al_2O_3 is employed in the fabrication, serving both as an interlayer (~ 1 nm) at the metal/Ge interface and an etch-stop layer (~ 20 nm) between the SiN_x and Ge. The former unpins the Fermi level of Ge from its valence band edge⁴⁹ for an elevated Schottky barrier height (Supplementary Fig. S12) and consequently a suppressed dark current, while the latter avoids an undesired etching of Ge during the SiN_x removal at its top⁵⁰. A top-view SEM image of a recessed SiN_x -strained device is shown in Fig. 3b, and the cross-sectional FIB-SEM images of the devices without and with the use of the recessed stressor are shown at the left of Fig. 3e, f, respectively. There is no observable delamination of SiN_x stressors from the Ge sidewalls, indicating a good device fabrication. The current-voltage (I-V) characteristics of the recessed detector, both with and without normal-incidence illumination of 20 mW laser power at 1,550 nm, were measured and the results are displayed in Fig. 3c. An explanation of the measurement set-up can be found in Methods. Dark currents of ~ 9.86 and ~ 41.70 μA were observed at biases of 1 and 2 V, respectively, while the illumination leads to prominent photocurrents of ~ 1.18 and ~ 2.01 mA accordingly. Considering the Ge effective absorption area under the optical fiber tip (tip diameter ~ 9 μm) without metal shielding, an optical responsivity of ~ 1.6 A/W was obtained at 2 V, corresponding to an internal quantum efficiency (IQE) of $\sim 129\%$ (Fig. 3c). Compared to that of the reference detectors without stressor, the IQE is significantly enhanced (Supplementary Fig. S14). As the only difference in fabrication between the two devices lies in the introduction of SiN_x , the IQE enhancement can be attributed to the defect and trap states in the SiN_x , due to its nonstoichiometric (nitrogen-rich) nature from both the ellipsometry measurement (Supplementary Fig. S4) and the low SiH_4/NH_3 ratio used in the deposition (Supplementary Table S2). Moreover, PECVD-deposited SiN_x films are commonly reported with heavy hydrogen (H-) incorporation⁵¹. The trap and defect states induce image carriers accumulated at the $\text{Ti}/\text{Al}_2\text{O}_3/\text{Ge}$ metal-insulator-semiconductor (MIS) interfaces, forming interfacial dipoles and fixed charge. This can be explained by the Schottky barrier height lowering of the MIS contact with the use of the SiN_x stressor (Supplementary Fig. S12), which had been correlated to the formation of interfacial dipoles⁵² and fixed charge⁵³ at MIS contacts in earlier studies. Meanwhile, these dipoles and charge enhance the electric field across the Al_2O_3 interlayer, contributing to an easier transport of photon-generated carriers across the interlayer and consequently a higher IQE. A supporting evidence to this claim comes from an earlier onset of Poole-Frenkel emission in the SiN_x -strained detector (Supplementary Fig. S15). The IQE $> 100\%$ indicates the existence of a photocurrent gain. The gain is unlikely originated from the interfacial charge as previously reported for MSM photodetectors⁵⁴ that induces an injection of extra image carriers into the device for a charge neutrality. This argument is based on the observation from the electric field simulation (Supplementary Fig. S16) indicating that the carrier transport in Ge had reached its saturation velocity ($\sim 6 \times 10^6$ cm/s) at a low bias of 0.3 V, implying a full collection of photon-generated carriers and a saturated IQE. However, this is inconsistent with the increasing, and $< 100\%$, IQE with an increasing bias observed in Fig. 3c and Supplementary Fig. S14. This suggests that the photocurrent is hindered by the Al_2O_3 barrier and the barrier does not provide a gain mechanism to the photocurrent. Further observation

finds that the gain can be attributed to the avalanche multiplication in Ge, since the electric field at 2 V (~ 180 kV/cm), compared to that in literature⁵⁵, is sufficiently high to impose avalanche amplification (Supplementary Fig. S16).

Fig. 3d shows the photocurrent spectra of the MSM photodetectors from 1,500 to 1,630 nm, covering the *C*- and *L*-bands (1,530–1,625 nm). In contrast to the photocurrent roll-off at $\sim 1,540$ nm for the Ge detector without stressor, a prominent drop of the photocurrent appears at longer wavelengths of 1,606 and 1,612 nm for SiN_x-strained detectors without and with the use of the recessed-type stressor, respectively. The roll-off points of the photocurrents have been identified as the Ge direct bandgap edges at the *G*-valley that determine the efficiency of direct-band absorption⁵⁶. The ~ 70 nm roll-off extension, along with the relatively flat spectra before the roll-off, indicates an enhanced detector quantum efficiency similar to that at the *C*-band covering most of the *L*-band. A further observation finds that there are additional distinguishable roll-off points at $\sim 1,580$ and $\sim 1,615$ nm for the non-recessed SiN_x-strained detector. This again demonstrates the strain non-uniformity in the Ge photodetectors without the use of the recessed SiN_x stressor. To investigate the correlation between the absorption coverage extension and the strain-induced Ge bandgap shrinkage, deformation potential theory⁵⁷ was utilized to calculate the Ge *G*-valley-light-hole (*G*-LH) and *G*-valley-heavy-hole (*G*-HH) bandgap edges as a function of the transverse strain, shown as the blue solid and red dotted lines, respectively, in Fig. 3g. The detailed calculation procedure is discussed in Supplementary section S11. A constant longitudinal strain of 0.17% was employed based on the earlier studies (Supplementary Fig. S2). Additionally, to estimate the Ge tensile strain in the SiN_x-strained detectors, the finite element simulation as described in Supplementary section S2 was performed by constructing the material and geometrical structures identical to that fabricated (Fig. 3e, f (both at left)). The tensile stress in SiN_x (600 MPa) is also identical. The simulated profiles are shown in Fig. 3e, f (both at right). As expected, a uniform of $\sim 0.42\%$ is obtained for the recessed SiN_x-strained *w*-Ge-OI, while the non-recessed stressor results in a two-step profile of $\sim 0.35\%$ at the upper part of Ge and $\sim 0.23\%$ at the lower part. Combining these results, the calculated Ge bandgap edges at the respective simulated (Fig. 3g) reasonably match with that observed from the photocurrent spectra in Fig. 3d. Subsequently, the simulated was used to calculate the absorption coefficient (*a*) enhancement of Ge, based on the photocurrent spectra. The detailed calculation is discussed in Supplementary section S10. Compared to the *a* ($2,265$ cm⁻¹) of the *w*-Ge-OI without stressor, the *a* ($7,474$ cm⁻¹) is enhanced by $\sim 3.3\times$ for the recessed SiN_x-strained *w*-Ge-OI at 1,612 nm, which is comparable with that of In_{0.53}Ga_{0.47}As material at the same wavelength⁵⁸. This suggests Ge photodetectors could reach a similar optoelectronic performance as InGaAs detectors and extend its application into prevailing III-V-dominated fields such as short-wave infrared imaging. In addition, the $3.3\times$ increase on *a* implies a $\sim 70\%$ reduction on the photon penetration depth ($\propto 1/a$) in Ge. The detector could consequently become more compact (a $\sim 70\%$ reduction in length and capacitance) with a commensurate photon absorption, alleviating the common responsivity-bandwidth trade-off. A maximum $3.3\times$ enhancement of the 3-dB bandwidth can be expected, provided that the device is limited by RC delay. It is also worthwhile to note that the equivalent *a* ($6,000$ cm⁻¹) for the *w*-Ge-OI without stressor at 1,500 nm is extended by 120 nm towards 1,620 nm for the

recessed SiN_x -strained w -Ge-OI, covering almost the entire C - and L -bands. This indicates that the performance of a Ge photodetector at 1,620 nm with the use of the recessed SiN_x stressor can be comparable to that at 1,500 nm without stressor. More channels at the L -band could thus be incorporated into the PIC design using the WDM scheme for a higher data capacity.

Broadband strained $\text{Ge}_{0.99}\text{Si}_{0.01}$ EA modulator arrays

The ultra-broadband EA modulation is demonstrated on a $\text{Ge}_{0.99}\text{Si}_{0.01}$ on SOI platform via the design and fabrication of SiN_x -strained waveguide-integrated $\text{Ge}_{0.99}\text{Si}_{0.01}$ modulator arrays. The reason for the $\sim 1\%$ Si incorporation in Ge is to position the broadband modulation with both tensile (~ 600 MPa) and compressive (~ 1 GPa) SiN_x stressors within the available tunable laser spectrum (1,510–1,610 nm) of our measurement system. Fig. 4a shows a schematic of an individual modulator and its working principle utilizing the Franz-Keldysh (FK) effect. The inset shows an optical microscope image of a fabricated device. Waveguide-shaped $\text{Ge}_{0.99}\text{Si}_{0.01}$ mesas (~ 300 nm-thick, $50 \mu\text{m}$ -long) were placed on top of Si-OI waveguides (~ 250 nm-thick) with tapers on both ends for efficient optical coupling into and out of the modulators (Fig. 4b). The Si waveguides are cross-sectionally in rib shape (Fig. 4c (right)) with a slab thickness of 80 nm to allow for a bottom contact of the modulators and form the recessed trenches for the SiN_x stressor for enhanced and uniform (Fig. 2d–f, h) transverse strain across the $\text{Ge}_{0.99}\text{Si}_{0.01}$ waveguide mesas. To facilitate the broadband modulation, the waveguide mesa width is varied (0.4, 0.7, 2.0, and $4.0 \mu\text{m}$) to engineer the $\text{Ge}_{0.99}\text{Si}_{0.01}$ strain and, consequently, its bandgap and operating wavelength coverage in response to an identical SiN_x stressor. As seen in Fig. 4c (left panel), a similar finite element simulation (Supplementary section S2) shows distinct transverse tensile strain (ϵ) profiles ranging from ~ 0.20 to $\sim 0.50\%$ with decreasing $\text{Ge}_{0.99}\text{Si}_{0.01}$ widths from 4.0 to $0.4 \mu\text{m}$, at an identical recessed tensile SiN_x stressor of 600 MPa. In the device fabrication, the SiN_x stressors were deposited via multi-frequency PECVD under controlled conditions (Supplementary section S4). A detailed description of the fabrication process can be found in Supplementary section S12. The dark current-voltage characteristics and a cross-sectional SEM image of a fabricated modulator are shown in Supplementary Fig. S17. To evaluate the modulator performance, optical transmission measurements (see Methods and Supplementary Fig. S18) were performed as a function of DC voltage bias. The lower maximum transmission at a wider $\text{Ge}_{0.99}\text{Si}_{0.01}$ width is due to the higher insertion loss (IL, ~ 5 dB) from the corresponding wider $\text{Ge}_{0.99}\text{Si}_{0.01}$ mesa (Fig. 4d). The extinction ratio (ER) spectra were then generated based on the transmission contrast of the modulators between 0 (on-state) and a reverse bias of -4 V (off-state) (Fig. 4e). A significant red-shift of the ER spectra is observed for the tensile-strained $\text{Ge}_{0.99}\text{Si}_{0.01}$ modulators with a decreasing $\text{Ge}_{0.99}\text{Si}_{0.01}$ width. The spectra ranges are consistent with the $\text{Ge}_{0.99}\text{Si}_{0.01}$ bandgap edge wavelengths from $\sim 1,520$ to $\sim 1,570$ nm at the corresponding widths, obtained from both the fitting of the optical transmission spectra (Fig. 4d) using the generalized FK model⁵⁹, and the deformation potential theory calculation (Supplementary section S11) according to the respective profiles (Fig. 4c (left panel)). Similarly, an increasing compressive can be expected with a decreasing

$\text{Ge}_{0.99}\text{Si}_{0.01}$ width, which explains the observable blue-shift of the ER spectra for the compressive-strained modulators. The spectra are not completely visible due to the limited measurement window.

The operating wavelength range of individual modulators is important for the arrayed broadband modulation. Here, the ER/IL ratio, as figure-of-merit (FOM), of 1.3 is considered to determine the modulator operating coverage. This is because, besides ER, IL also increases with decreasing wavelength due to the increased Ge-based direct-band absorption. The value of 1.3 is reasonable among the values (0.8–1.7) reported in prior studies^{24, 25, 26, 60} and foundry PDK standards for high-speed optical interconnect applications⁶¹. Using this criterion, the operating coverage of a tensile $\text{Ge}_{0.99}\text{Si}_{0.01}$ modulator (50- μm long, 0.7- μm wide) extends from $\sim 1,580$ to $\sim 1,610$ nm, where the IL is < 6.8 dB. The operating optical bandwidth of individual modulators generally spans $\sim 27.5 \pm 3.5$ nm at -6 V within the measurement window and is independent of the strain. The operating wavelength coverages for modulators beyond the measurement window were estimated based on the corresponding bandgap edge wavelengths obtained from the optical transmission measurements with the span of the determined average optical bandwidth. The individual spectra overlap and form an ultra-broadband wavelength coverage ranging from $\sim 1,460$ to $\sim 1,620$ nm at -6 V, where the compressive and tensile modulators cover from $\sim 1,460$ to $\sim 1,530$ nm and $\sim 1,525$ to $\sim 1,620$ nm, respectively (Fig. 4f). The modulator insertion loss can be reduced to ~ 2 dB via the optimization of top Si electrodes and taper coupling design⁶², which could further increase the ER/IL performance and reduce the operating voltage and modulation dynamic power of the modulator.

Broadband Ge-based modulator-detector co-integration

To investigate the feasibility of the Ge-based modulator-detector co-integration in a single step of Ge-based epitaxy (Fig. 1), a 1-GPa recessed compressive SiN_x stressor was introduced to an array of Ge waveguide-mesas on Si-OI waveguides similar to the design in Fig. 4. Similar optical transmission measurements were performed. As expected, the transmission started to increase at a shorter wavelength with decreasing mesa width, indicating an increase of the Ge bandgap due to the higher compressive strain in a narrower mesa (Fig. 5a). The FK model fitting (Fig. 5a, solid curves) agrees well with the transmission spectra (circled dots) and extracts the strain and bandgap information in Ge (Supplementary Table 2). The ER spectra were then calculated (see Methods), as shown in Fig. 5b. The predicted operating coverage for the Ge modulator array ranges from $\sim 1,520$ to 1,630 nm. Overlaying with the absorption spectrum (Fig. 3d) of the tensile-strained Ge photodetector provides a broad wavelength window of over 100 nm for the Ge modulator-detector co-integration. The small footprint of the SiN_x stressor (Supplementary section S7) provides the convenience to separately use tensile and compressive stressors on the photodetectors and modulator arrays, respectively, for the co-integration. Additionally, with an increasing Si incorporation, the bandgap of GeSi shrinks, which will shift the broad co-integration bandwidth to shorter wavelengths. Bandgap (see Methods) and FK model calculation finds that 1% Si incorporation will shift the co-integrated optical bandwidth range to $\sim 1,460$ –1,575 nm, covering *E*- and *C*-bands (Fig. 5c). A 4% Si incorporation further shifts the co-integrated optical

wavelength range to *O*- and *E*-bands (1,300–1,450 nm), where the FK effect remains significant since the direct-band transition dominates at the Γ -valley.

Conclusion

In conclusion, strained Ge photodetectors and $\text{Ge}_{0.99}\text{Si}_{0.01}$ EA modulator arrays have been demonstrated with ultra-broad operating wavelength range. The photodetectors demonstrate a considerable Ge absorption coefficient ($>4,000 \text{ cm}^{-1}$) up to 1,630 nm and the $\text{Ge}_{0.99}\text{Si}_{0.01}$ modulator arrays exhibit an operating wavelength range of ~ 100 nm where the ER/IL >1.3 , from $\sim 1,525$ –1,620 nm. The broadband operation also enables the co-integration of Ge-based photodetectors and EA modulators using one Ge composition, with an overlapping operating window over 100 nm. Si incorporation up to 4% is expected to shift the broad modulation and co-integration coverages to as short as 1,300 nm, and Sn incorporation to longer wavelengths beyond 1,700 nm. The broadband device operations are realized by simple and cost-effective process integration requiring only a single-step Ge-based epitaxy and recessed-type SiN_x stressors, both of which are matured processes in state-of-the-art foundries. In particular, the recessed feature of the stressor results in a uniform and enhanced strain profile in the Ge-based materials to further extend the device operating coverage. This work paves the way towards high-data-capacity and low-cost PICs for future dense wavelength-division multiplexing (DWDM) computing and data center networks as well as a myriad of other emerging applications.

Methods

Micro-Raman measurement and its calibration

Micro-Raman measurements were performed using commercial systems (WITec UHTS 300, Renishaw inVia, and HORIBA LabRAM HR) at longitudinal optical (LO) mode via confocal backscattering configuration at laser emitting wavelengths of 532 and 785nm. The objective lens used are 100 \times , with numerical apertures at 0.9 (for WITEC and HORIBA) and 0.75 (for Renishaw). The diameter of the laser spots is $\sim 1 \mu\text{m}$. The backscattered signal went through a spectrometer and was collected by CCD detectors to form Raman spectra. The output power of the lasers was set to have a negligible heating effect on the samples. The spectra at different system and wavelengths were aligned based on their Si peaks ($\sim 520.6 \text{ cm}^{-1}$) for comparison. The obtained spectra were fitted by Lorentzian function to determine their peak positions for further analysis (Fig. S3b).

Photodetector characterization

The current-voltage (I-V) characteristics of the photodetectors were measured by an Aim-TTi QL355TP power supply and a Keysight 34450A multimeter. To measure the optical response, a TUNICS T100S-HP/CL tunable laser covering *C*- and *L*-bands (1500 to 1630 nm) was utilized as the light source. Light was out-coupled into a Corning SMF-28 single-mode silica glass fiber to illuminate on the devices. The dark I-V curves were also collected as a function of temperature ranging from 293 to 353 K.

EA modulator array performance characterization and ER and GeSi bandgap calculation

Optical transmission measurement was performed using an optical vector analyzer (OVA), comprising a tunable laser (1,510–1,610 nm) and a detector from Luna technologies (Luna Innovations Inc.), as seen in Supplementary Fig. S18. Light was butt-coupled into and out of the guiding Si-OI waveguides to modulators via cleaved facets. Difference in the transmitted optical power was recorded between a modulator at 0 V and a reference Si-OI waveguide identical to that in the modulator as the device insertion loss. Electrical probes were probed on the device metal pads to source DC voltage bias during the optical transmission measurement to obtain the device extinction ratio (ER). For the ER calculation in Fig. 5b, an electric field contrast between 40 (off-state) and 10 (built-in field, on-state) kV/cm was considered in the FK modelling, which corresponds to reverse bias voltages of -3 and 0 V, respectively. The built-in electric field of 10 kV/cm is due to the Fermi-level equalization between Ge and Si substrate. The GeSi bandgaps are estimated according to a linear interpolation of L -, G -, and X -valley bandgaps of Ge and Si. For a small Si composition of less than $\sim 5\%$, the direct bandgap E_g^G is smaller than the indirect bandgap E_g^X and the FK effect at the direct bandgap dominates. The simulated photodetector coverages were determined by the calculated bandgap edges of the corresponding strained Ge-based materials.

Declarations

Acknowledgements

This research project is supported by the National Research Foundation, Singapore, under its Competitive Research Program (CRP Award NRF-CRP19-2017-01). The authors are grateful for the financial support from the Singapore-MIT Alliance for Research and Technology's (SMART) Low Energy Electronic Systems (LEES) IRG. The authors would also like to thank the technical support from the Nanyang Nanofabrication center (N2FC) at NTU and the MIT Nano and Substrate Engineering Lab cleanroom facilities at MIT for the device fabrication; and X. Guo and J. Zhou's support in Prof. H. Wang's group at NTU on the testing and EBL patterning of strained Ge-OI photodetectors. The acknowledgement also goes to W.J. Wang and S. Liu at NTU SPMS for the Raman measurements and D.M. Weninger for the drawing of Fig. 1. Y.L acknowledges the financial support from the SMART Fellowship.

Author contributions

Y.L and J.M conceived the idea. Y.L and D.M performed the simulation. Y.L designed and fabricated the strained w -Ge-OIs and photodetectors and performed characterizations and data analysis. D.M designed and fabricated the strained EA modulator arrays and performed characterizations and data analysis. R-T.W and K.H.L prepared Ge- and $\text{Ge}_{0.99}\text{Si}_{0.01}$ -on-SOI and Ge-OI wafers for device fabrication. R-T.W and G.S carried out FIB imaging of the devices. Y.L, D.M and J.M composed and revised the manuscript. L.C.K, C.S.T and J.M supervised and supported the work. All authors proofread the manuscript.

Competing financial interests

The authors declare no competing financial interests.

References

1. Miller DAB. Optical interconnects to electronic chips. *Appl Opt* 2010, **49**(25): F59-F70.
2. Taubenblatt MA. Optical Interconnects for High-Performance Computing. *Journal of Lightwave Technology* 2012, **30**(4): 448-457.
3. Subramanian AZ, Ryckeboer E, Dhakal A, Peyskens F, Malik A, Kuyken B, *et al.* Silicon and silicon nitride photonic circuits for spectroscopic sensing on-a-chip [Invited]. *Photonics Research* 2015, **3**(5).
4. Soref R. Mid-infrared photonics in silicon and germanium. *Nature Photonics* 2010, **4**(8): 495-497.
5. Orieux A, Diamanti E. Recent advances on integrated quantum communications. *Journal of Optics* 2016, **18**(8).
6. Sibson P, Erven C, Godfrey M, Miki S, Yamashita T, Fujiwara M, *et al.* Chip-based quantum key distribution. *Nature communications* 2017, **8**: 13984.
7. Zhang G, Haw JY, Cai H, Xu F, Assad SM, Fitzsimons JF, *et al.* An integrated silicon photonic chip platform for continuous-variable quantum key distribution. *Nature Photonics* 2019, **13**(12): 839-842.
8. Vandoorne K, Mechet P, Van Vaerenbergh T, Fiers M, Morthier G, Verstraeten D, *et al.* Experimental demonstration of reservoir computing on a silicon photonics chip. *Nature communications* 2014, **5**: 3541.
9. Shen Y, Harris NC, Skirlo S, Prabhu M, Baehr-Jones T, Hochberg M, *et al.* Deep learning with coherent nanophotonic circuits. *Nature Photonics* 2017, **11**(7): 441-446.
10. Feldmann J, Youngblood N, Wright CD, Bhaskaran H, Pernice WHP. All-optical spiking neurosynaptic networks with self-learning capabilities. *Nature* 2019, **569**(7755): 208-214.
11. Welkenhuysen M, Hoffman L, Luo Z, De Proft A, Van den Haute C, Baekelandt V, *et al.* An integrated multi-electrode-optrode array for in vitro optogenetics. *Scientific reports* 2016, **6**: 20353.
12. Sacher WD, Liu X, Chen F-D, Moradi-Chameh H, Almog IF, Lordello T, *et al.* Beam-Steering Nanophotonic Phased-Array Neural Probes. Conference on Lasers and Electro-Optics; 2019 2019/05/05; San Jose, California: Optical Society of America; 2019. p. AT41.4.
13. RP Photonics Encyclopedia - silica fibers, optical fiber, glass, fiber optics. [cited 18 June 2020] Available from: https://www.rp-photonics.com/silica_fibers.html
14. Ishikawa Y, Wada K, Liu J, Cannon DD, Luan H-C, Michel J, *et al.* Strain-induced enhancement of near-infrared absorption in Ge epitaxial layers grown on Si substrate. *Journal of Applied Physics* 2005, **98**(1): 013501.
15. Jongthammanurak S, Liu J, Wada K, Cannon DD, Danielson DT, Pan D, *et al.* Large electro-optic effect in tensile strained Ge-on-Si films. *Applied Physics Letters* 2006, **89**(16): 161115.

16. Liu J, Michel J, Giziewicz W, Pan D, Wada K, Cannon DD, *et al.* High-performance, tensile-strained Ge p-i-n photodetectors on a Si platform. *Applied Physics Letters* 2005, **87**(10): 103501.
17. Yin T, Cohen R, Morse MM, Sarid G, Chetrit Y, Rubin D, *et al.* 31GHz Ge n-i-p waveguide photodetectors on Silicon-on-Insulator substrate. *Optics express* 2007, **15**(21): 13965-13971.
18. Michel J, Liu J, Kimerling LC. High-performance Ge-on-Si photodetectors. *Nature Photonics* 2010, **4**(8): 527-534.
19. Virost L, Vivien L, Fédéli J-M, Bogumilowicz Y, Hartmann J-M, Bœuf F, *et al.* High-performance waveguide-integrated germanium PIN photodiodes for optical communication applications [Invited]. *Photonics Research* 2013, **1**(3): 140.
20. Chen H, Verheyen P, De Heyn P, Lepage G, De Coster J, Balakrishnan S, *et al.* 1 V bias 67 GHz bandwidth Si-contacted germanium waveguide p-i-n photodetector for optical links at 56 Gbps and beyond. *Optics express* 2016, **24**(5): 4622-4631.
21. Liu J, Beals M, Pomerene A, Bernardis S, Sun R, Cheng J, *et al.* Waveguide-integrated, ultralow-energy GeSi electro-absorption modulators. *Nature Photonics* 2008, **2**(7): 433-437.
22. Feng N-N, Feng D, Liao S, Wang X, Dong P, Liang H, *et al.* 30GHz Ge electro-absorption modulator integrated with 3 μ m silicon-on-insulator waveguide. *Optics express* 2011, **19**(8): 7062-7067.
23. Feng D, Liao S, Liang H, Fong J, Bijlani B, Shafiiha R, *et al.* High speed GeSi electro-absorption modulator at 1550 nm wavelength on SOI waveguide. *Optics express* 2012, **20**(20): 22224-22232.
24. Gupta S, Srinivasan SA, Pantouvaki M, Chen H, Verheyen P, Lepage G, *et al.* 50GHz Ge waveguide electro-absorption modulator integrated in a 220nm SOI photonics platform. 2015 Optical Fiber Communications Conference and Exhibition (OFC); 2015 22-26 March 2015; 2015. p. 1-3.
25. Srinivasan SA, Pantouvaki M, Gupta S, Chen HT, Verheyen P, Lepage G, *et al.* 56 Gb/s Germanium Waveguide Electro-Absorption Modulator. *Journal of Lightwave Technology* 2016, **34**(2): 419-424.
26. Mastronardi L, Banakar M, Khokhar AZ, Hattasan N, Rutirawut T, Bucio TD, *et al.* High-speed Si/GeSi hetero-structure Electro Absorption Modulator. *Optics express* 2018, **26**(6): 6663-6673.
27. Liao L, Samara-Rubio D, Morse M, Liu A, Hodge D, Rubin D, *et al.* High speed silicon Mach-Zehnder modulator. *Optics express* 2005, **13**(8): 3129-3135.
28. Green WMJ, Rooks MJ, Sekaric L, Vlasov YA. Ultra-compact, low RF power, 10 Gb/s silicon Mach-Zehnder modulator. *Optics express* 2007, **15**(25): 17106-17113.
29. Xu Q, Manipatruni S, Schmidt B, Shakya J, Lipson M. 12.5 Gbit/s carrier-injection-based silicon micro-ring silicon modulators. *Optics express* 2007, **15**(2): 430-436.
30. Manipatruni S, Xu Q, Schmidt B, Shakya J, Lipson M. High Speed Carrier Injection 18 Gb/s Silicon Micro-ring Electro-optic Modulator. LEOS 2007 - IEEE Lasers and Electro-Optics Society Annual Meeting Conference Proceedings; 2007 21-25 Oct. 2007; 2007. p. 537-538.
31. Tseng HH, Li H, Mashanov V, Yang YJ, Cheng HH, Chang GE, *et al.* GeSn-based p-i-n photodiodes with strained active layer on a Si wafer. *Applied Physics Letters* 2013, **103**(23): 231907.

32. Luo X, Cao Y, Song J, Hu X, Cheng Y, Li C, *et al.* High-throughput multiple dies-to-wafer bonding technology and III/V-on-Si hybrid lasers for heterogeneous integration of optoelectronic integrated circuits. *Frontiers in Materials* 2015, **2**: 28.
33. Justice J, Bower C, Meitl M, Mooney MB, Gubbins MA, Corbett B. Wafer-scale integration of group III-V lasers on silicon using transfer printing of epitaxial layers. *Nature Photonics* 2012, **6**(9): 610-614.
34. Chaisakul P, Marris-Morini D, Frigerio J, Chrastina D, Rouifed M-S, Cecchi S, *et al.* Integrated germanium optical interconnects on silicon substrates. *Nat Photon* 2014, **8**(6): 482-488.
35. Littlejohns CG, Nedeljkovic M, Mallinson CF, Watts JF, Mashanovich GZ, Reed GT, *et al.* Next generation device grade silicon-germanium on insulator. *Scientific reports* 2015, **5**: 8288.
36. Chu M, Sun Y, Aghoram U, Thompson SE. Strain: A Solution for Higher Carrier Mobility in Nanoscale MOSFETs. *Annual Review of Materials Research* 2009, **39**(1): 203-229.
37. Sacher WD, Luo X, Yang Y, Chen FD, Lordello T, Mak JCC, *et al.* Visible-light silicon nitride waveguide devices and implantable neurophotonic probes on thinned 200 mm silicon wafers. *Optics express* 2019, **27**(26): 37400-37418.
38. Süess MJ, Geiger R, Minamisawa RA, Schiefler G, Frigerio J, Chrastina D, *et al.* Analysis of enhanced light emission from highly strained germanium microbridges. *Nature Photonics* 2013, **7**(6): 466-472.
39. Nam D, Sukhdeo D, Roy A, Balram K, Cheng S-L, Huang KC-Y, *et al.* Strained germanium thin film membrane on silicon substrate for optoelectronics. *Optics express* 2011, **19**(27): 25866-25872.
40. de Kersauson M, Prost M, Ghrib A, El Kurdi M, Sauvage S, Beaudoin G, *et al.* Effect of increasing thickness on tensile-strained germanium grown on InGaAs buffer layers. *Journal of Applied Physics* 2013, **113**(18): 183508.
41. Wu H, Ye PD. Fully Depleted Ge CMOS Devices and Logic Circuits on Si. *IEEE Transactions on Electron Devices* 2016, **63**(8): 3028-3035.
42. Lin Y, Lee KH, Bao S, Guo X, Wang H, Michel J, *et al.* High-efficiency normal-incidence vertical p-i-n photodetectors on a germanium-on-insulator platform. *Photonics Research* 2017, **5**(6): 702-709.
43. Li W, Anantha P, Bao S, Lee KH, Guo X, Hu T, *et al.* Germanium-on-silicon nitride waveguides for mid-infrared integrated photonics. *Applied Physics Letters* 2016, **109**(24): 241101.
44. Kang J, Takenaka M, Takagi S. Novel Ge waveguide platform on Ge-on-insulator wafer for mid-infrared photonic integrated circuits. *Optics express* 2016, **24**(11): 11855-11864.
45. Lee KH, Bao S, Chong GY, Tan YH, Fitzgerald EA, Tan CS. Fabrication and characterization of germanium-on-insulator through epitaxy, bonding, and layer transfer. *Journal of Applied Physics* 2014, **116**(10): 103506.
46. Lee KH, Bao S, Chong GY, Tan YH, Fitzgerald EA, Tan CS. Defects reduction of Ge epitaxial film in a germanium-on-insulator wafer by annealing in oxygen ambient. *APL Materials* 2015, **3**(1): 016102.
47. Woo Sik Yoo KK, Takeshi Ueda, Toshikazu Ishigaki, Hiroshi Nishigaki, Noriyuki Hasuike, Hiroshi Harima, Masahiro Yoshimoto, and Chuan Seng Tan. Detection of Ge and Si Intermixing in Ge/Si using Multiwavelength Micro-Raman Spectroscopy. *ECS Transactions* 2014, **64**(6): 79-88.

48. Tsao C-Y, Weber JW, Campbell P, Widenborg PI, Song D, Green MA. Low-temperature growth of polycrystalline Ge thin film on glass by in situ deposition and ex situ solid-phase crystallization for photovoltaic applications. *Applied Surface Science* 2009, **255**(15): 7028-7035.
49. Zhou Y, Ogawa M, Han X, Wang KL. Alleviation of Fermi-level pinning effect on metal/germanium interface by insertion of an ultrathin aluminum oxide. *Applied Physics Letters* 2008, **93**(20): 202105.
50. Kolari K. High etch selectivity for plasma etching SiO₂ with AlN and Al₂O₃ masks. *Microelectronic Engineering* 2008, **85**(5): 985-987.
51. Mao SC, Tao SH, Xu YL, Sun XW, Yu MB, Lo GQ, *et al.* Low propagation loss SiN optical waveguide prepared by optimal low-hydrogen module. *Optics express* 2008, **16**(25): 20809-20816.
52. Lin L, Li H, Robertson J. Control of Schottky barrier heights by inserting thin dielectric layers. *Applied Physics Letters* 2012, **101**(17).
53. Hu J, Nainani A, Sun Y, Saraswat KC, Philip Wong HS. Impact of fixed charge on metal-insulator-semiconductor barrier height reduction. *Applied Physics Letters* 2011, **99**(25).
54. Klingenstein M, Kuhl J, Rosenzweig J, Moglestue C, Hülsmann A, Schneider J, *et al.* Photocurrent gain mechanisms in metal-semiconductor-metal photodetectors. *Solid-State Electronics* 1994, **37**(2): 333-340.
55. Assefa S, Xia F, Vlasov YA. Reinventing germanium avalanche photodetector for nanophotonic on-chip optical interconnects. *Nature* 2010, **464**(7285): 80-84.
56. Liu J, Cannon DD, Wada K, Ishikawa Y, Jongthammanurak S, Danielson DT, *et al.* Tensile strained Ge p-i-n photodetectors on Si platform for C and L band telecommunications. *Applied Physics Letters* 2005, **87**(1): 011110.
57. Van de Walle CG. Band lineups and deformation potentials in the model-solid theory. *Physical Review B* 1989, **39**(3): 1871-1883.
58. Humphreys DA, King RJ, Jenkins D, Moseley AJ. Measurement of absorption coefficients of Ga_{0.47}In_{0.53}As over the wavelength range 1.0-1.7 μm. *Electronics Letters* 1985, **21**(25): 1187-1189.
59. Chuang SL. *Physics of photonic devices*, vol. 80. John Wiley & Sons, 2012.
60. Heyn PD, Srinivasan SA, Verheyen P, Loo R, Wolf ID, Balakrishnan S, *et al.* High-speed germanium-based waveguide electro-absorption modulator. 2016 21st OptoElectronics and Communications Conference (OECC) held jointly with 2016 International Conference on Photonics in Switching (PS); 2016 3-7 July 2016; 2016. p. 1-3.
61. Rakowski M. Silicon Photonics platform for 50G optical interconnects. Photonics Summit and Workshop 2017 [cited] Available from: https://www.cadence.com/content/dam/cadence-www/global/en_US/documents/company/Events/summits/photronics/rakowski-2017.pdf
62. Ma D. Ge and GeSi Electroabsorption Modulator Arrays via Strain and Composition Engineering. Doctor of Philosophy thesis, Massachusetts Institute of Technology 2020.

Figures

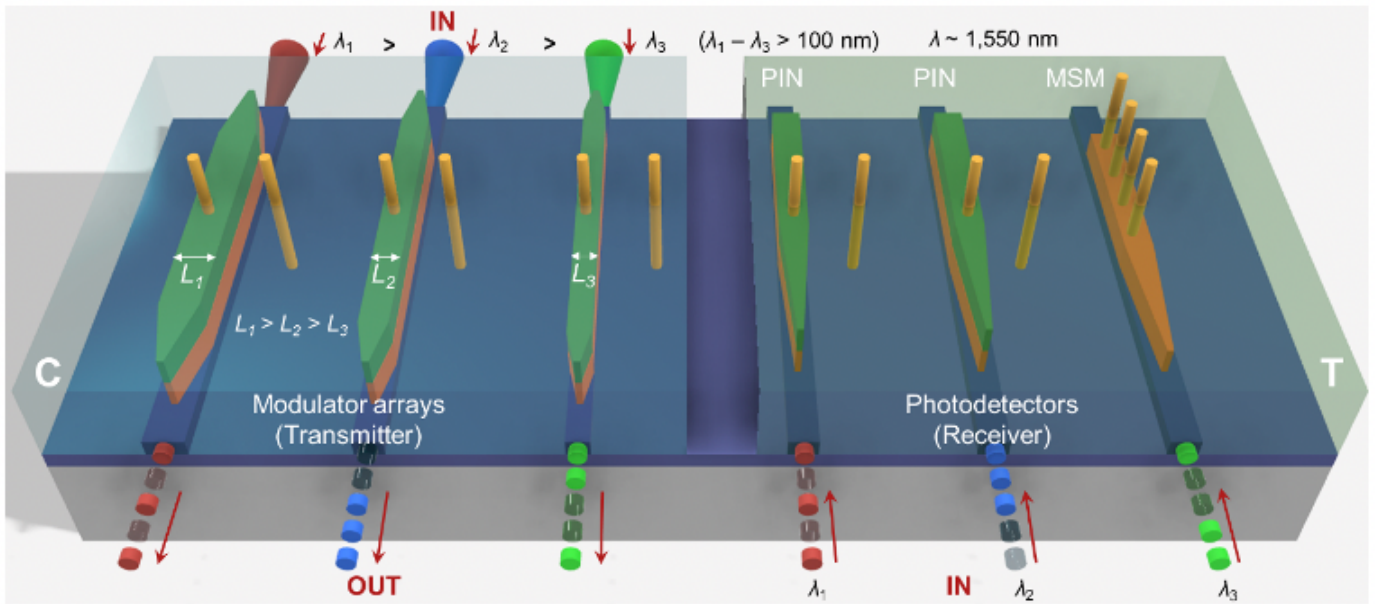


Figure 1

A schematic showing a co-integration of Ge-based EA modulator arrays and photodetectors for ultra-broadband and low-cost optical transceivers. Colour coded layers and labels: grey, SiO₂; blue, Si; orange, Ge-based material (Ge, GeSi or GeSn); green, poly-Si; gold, tungsten plugs; C, compressive SiN_x stressor; T, tensile SiN_x stressor; PIN, p-i-n photodetectors; MSM, metal-semiconductor-metal photodetectors; λ_1 , λ_2 , λ_3 , input wavelengths; L_1 , L_2 , L_3 , modulator mesa widths. The compressive and tensile stressors facilitate a broad common operating wavelength window for both the modulator arrays and photodetectors, requiring only a single step of Ge-based epitaxy at low integration cost.

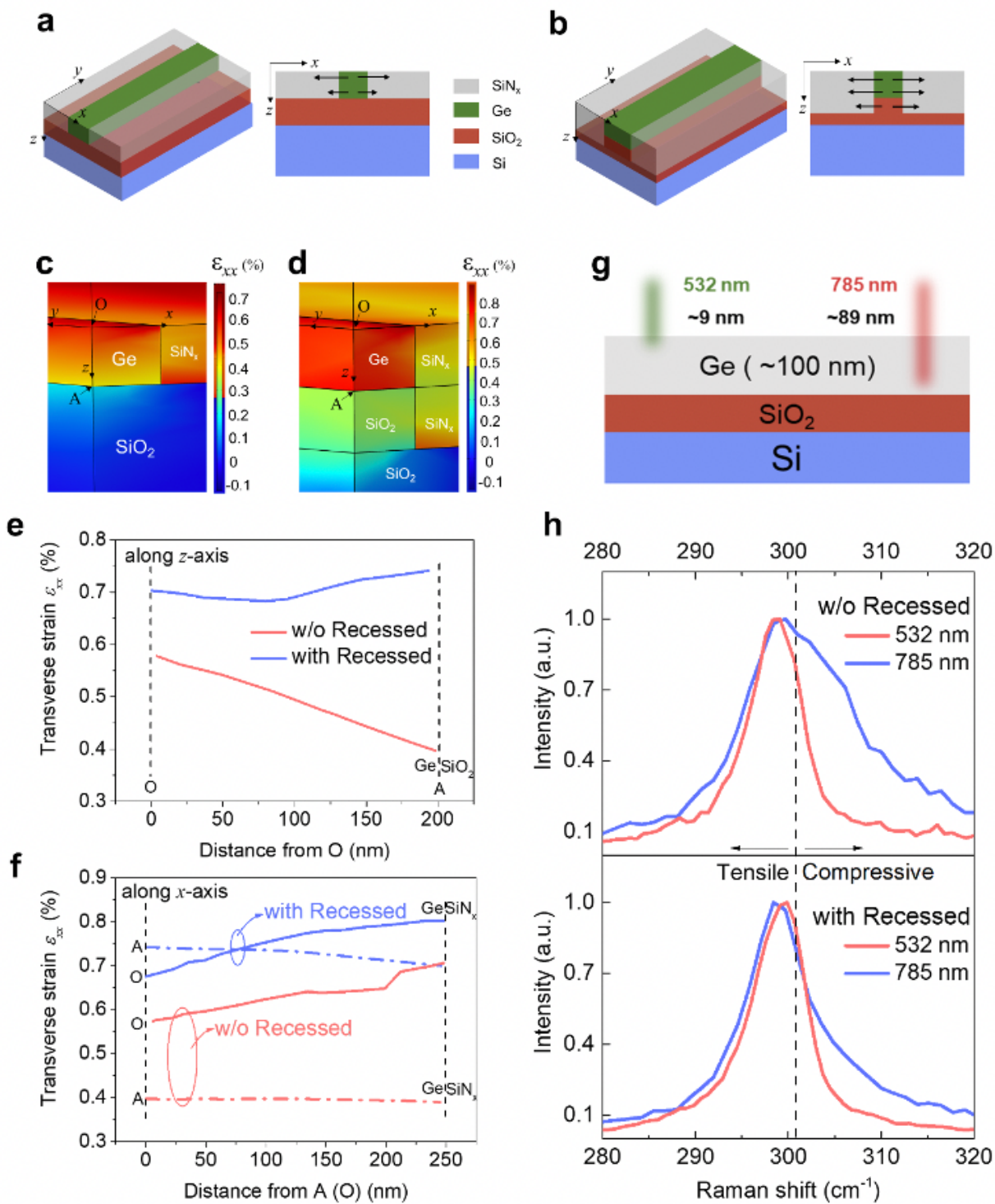


Figure 2

Finite element simulation and micro-Raman characterization of Ge mechanical strain, demonstrating the effect of recessed SiNx stressor: an example of tensile-stressed stressor on w-Ge-OI. a, b (Left) three-dimensional (3-D) schematics for layer structures of w-Ge-OI without (a) and with (b) the sidewall SiNx stressor recessed into the underlying SiO₂. (Right) Corresponding cross-sectional schematics, where the black solid arrows indicate a spatial distribution of the tensile strain in Ge along z-axis. c, d Simulated Ge

transverse mechanical strain (ϵ_{xx}) profiles without (c) and with (d) the SiNx stressor recessed. The profiles beyond Ge are artificial due to simulation settings. The width and height of Ge waveguides are 500 nm (due to the symmetry setting of the model, only 250 nm is shown) and 200 nm, respectively, and the tensile stress is 1 GPa in the SiNx stressor. The recessed trench depth is 200 nm into SiO₂ (in d). e, f Extracted Ge ϵ_{xx} values from the profiles in c and d with respect to the use of the recessed SiNx stressor, along z- (e) and x- (f) axes, where points O and A are also indicated accordingly. g A cross-sectional schematic of Ge-OI elucidating distinct photon penetration depths of ~ 9 and ~ 89 nm, respectively, at laser excitation wavelengths of 532 and 785 nm in micro-Raman measurements. h Micro-Raman spectra of w-Ge-OI at a width of 0.5 μm without (top) and with (bottom) the SiNx stressor recessed. The black dashed line corresponds to the peak LO phonon frequency ($\sim 300.8 \text{ cm}^{-1}$) of bulk Ge as a stress-free reference, beyond which a decrease and increase of the frequency indicate an enhancement of the tensile and compressive strain in Ge, respectively.

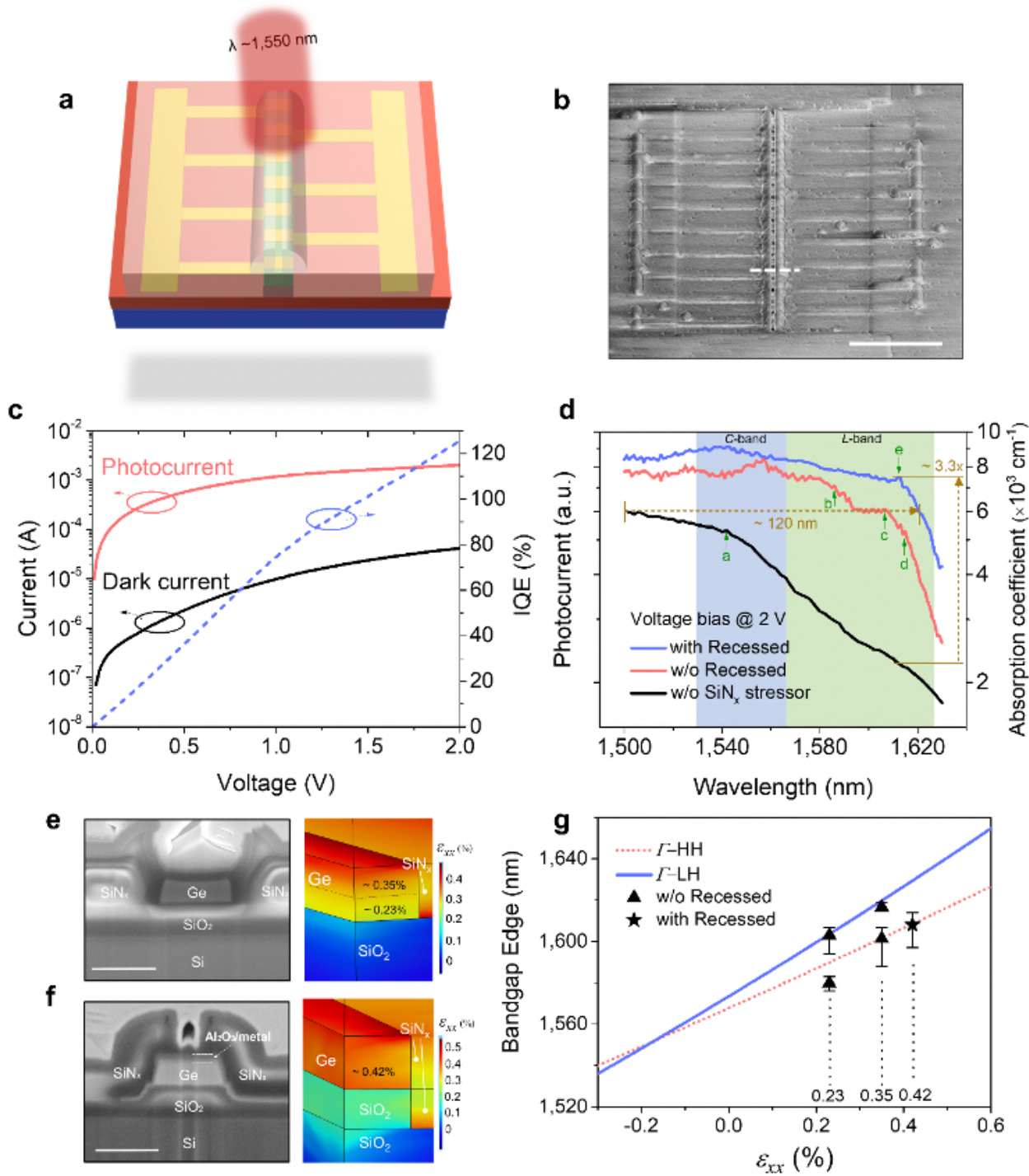


Figure 3

Performance of recessed SiNx-strained Ge-OI metal-semiconductor-metal (MSM) photodetectors and its correlation to the induced mechanical strain in Ge. a A 3-D schematic layer structure of a GOI MSM photodetector with the use of the recessed SiNx stressor. Colour coded layers: purple, Si; dark red, SiO₂; green, Ge; gold, contact metal; semi-transparent, tensile-stressed SiNx. Optical power was perpendicularly illuminated upon the device via a single-mode silica glass fiber. b An SEM image of a fabricated device

(top-down tilted view). Scale bar, 10 μm . c Current-voltage (I-V) characteristics of the device without (black) and with (red) an incident power of ~ 20 mW at 1,550 nm. The corresponding internal quantum efficiency (IQE) is also included as a function of biasing voltage. d Photocurrent spectra of GOI MSM photodetectors with respect to the use of the (recessed) SiNx stressor. Green arrows indicate respective roll-off points: a, 1,540 nm; b, 1,580 nm; c, 1,606 nm; d, 1,615 nm; e, 1,612 nm. The spectra were further utilized to extract strain-enhanced Ge effective absorption coefficient, shown as the right y-axis. e, f (Left) focused-ion beam (FIB)-prepared cross-sectional SEM images of devices and (right) their corresponding finite-element simulated Ge strain profiles without (e) and with (f) the use of the recessed SiNx stressor. Scale bar: 1 μm . g Correlation between the simulated Ge strain (in e and f, both at right) and the Ge bandgap edges from the photocurrent spectra (in d), according to the deformation potential theory.

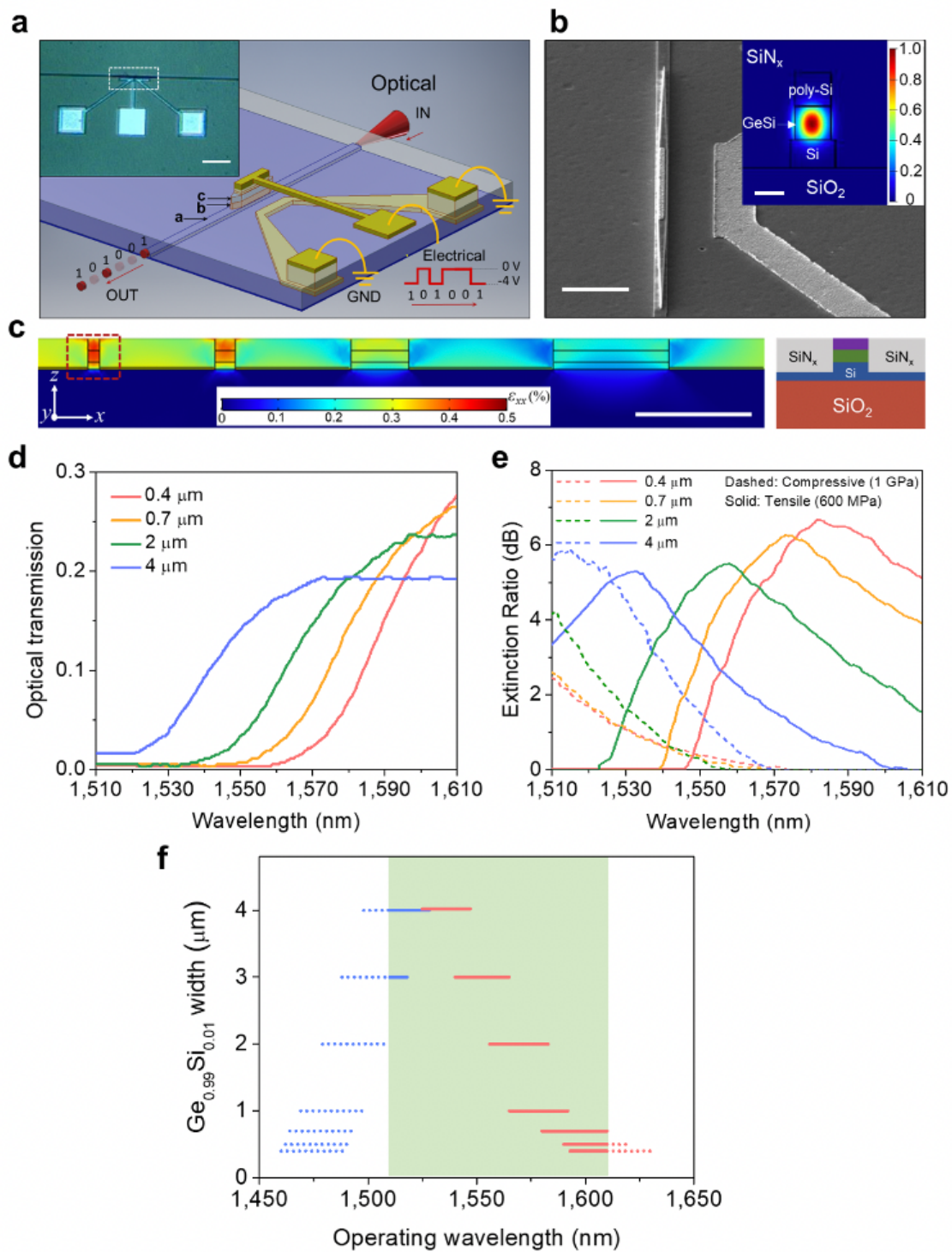


Figure 4

Ultra-broadband EA modulation enabled by recessed SiNx-strained Ge_{0.99}Si_{0.01} modulator arrays. **a** A schematic of an individual modulator and its working principle. Layer structures: purple, Si; semi-transparent, SiNx stressor; gold, contact metal; a, Si waveguide-OI; b, Ge_{0.99}Si_{0.01}; c, poly-Si. The SiO₂ and bulk Si layers of the SOI substrate are not drawn. Inset shows an optical microscope image of a fabricated device. Scale bar: 50 μm. **b** An SEM image of a Ge_{0.99}Si_{0.01} modulator (from the white dotted

area in the inset of a) in fabrication before the stressor deposition, showing a Ge_{0.99}Si_{0.01} waveguide-mesa on a Si-OI waveguide with tapers at both ends. Scale bar: 5 μm. Inset shows a fundamental TE mode in a Ge_{0.99}Si_{0.01} mesa at the wavelength of 1,550 nm. Scale bar: 400 nm. c (Left) finite element simulation of ϵ_{xx} in Ge_{0.99}Si_{0.01} mesas with different widths (0.4, 0.7, 2.0 and 4.0 μm) at an identical recessed tensile SiN_x stressor (600 MPa). Scale bar: 4 μm; (Right) a layer structure schematic from the red dashed box at left. Colour coded layers: purple, poly-Si; green, Ge_{0.99}Si_{0.01}. d Optical transmission spectra of the tensile SiN_x-strained Ge_{0.99}Si_{0.01} modulators at 0 V. e Extinction ratio of Ge_{0.99}Si_{0.01} modulators with tensile (600 MPa, solid curves) and compressive (1 GPa, dashed curves) recessed SiN_x stressors at a reverse bias of -4 V. f Operating wavelength coverage of strained (blue: 1-GPa compressive, red: 600-MPa tensile) individual modulators in the arrays at different Ge_{0.99}Si_{0.01} widths, based on the measurement (solid lines) and simulation (dotted lines) results at -6 V. The green rectangle indicates the measurement window (1,510–1,610 nm).

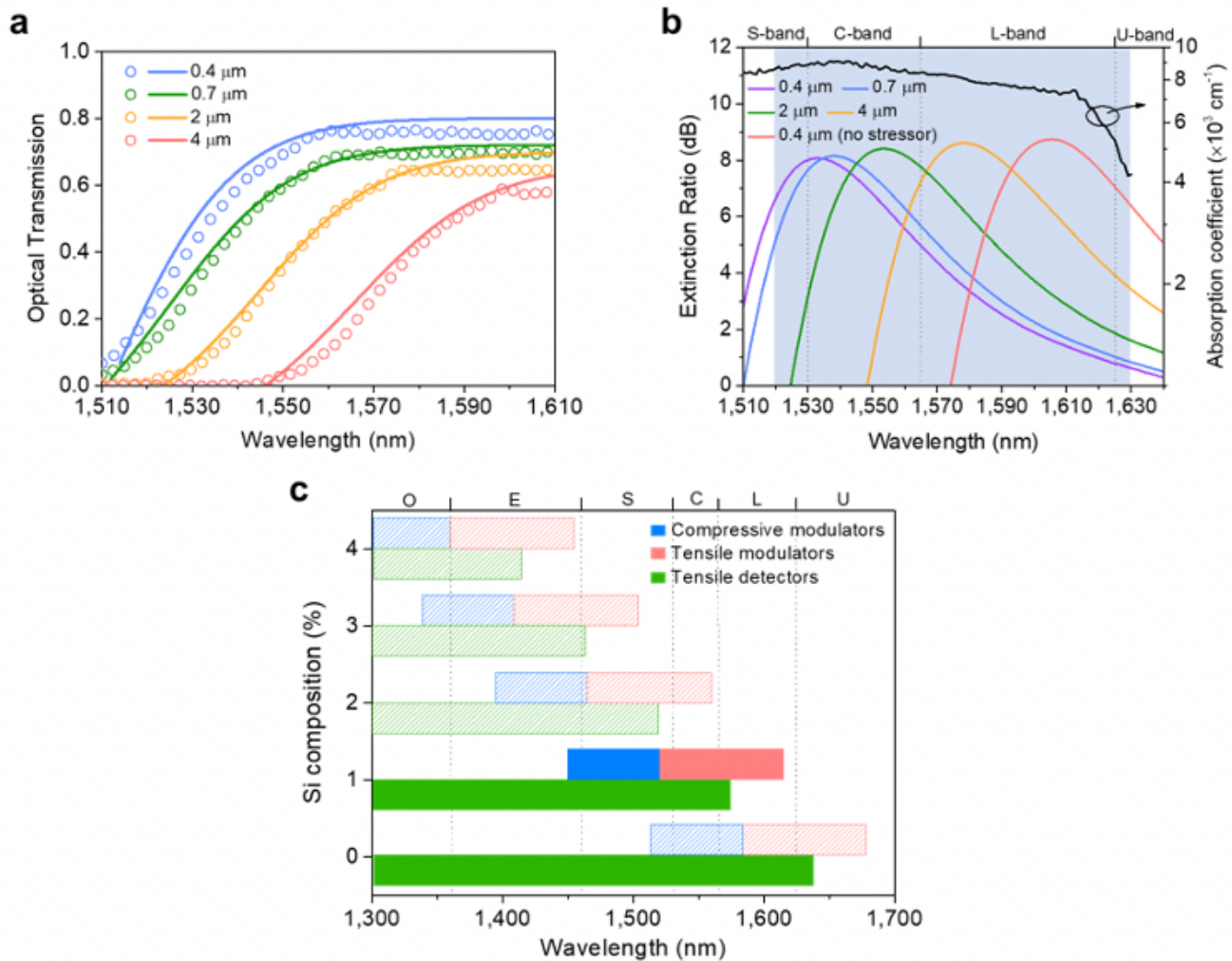


Figure 5

Envisioning ultra-broadband Ge-based EA modulator-detector co-integration. a Optical transmission spectra (circled dots) of compressive (~ 1 GPa) SiNx-strained Ge waveguide-mesas with different widths at 0 V, fitted with the generalized FK model (solid curves). b An overlaid absorption coefficient spectra of tensile (~ 600 MPa) SiNx-strained Ge photodetector (from Fig. 3d) and ER spectra of compressive (~ 1 GPa) SiNx-strained Ge EA modulator arrays (calculated from the FK fitting in a), showing the potential for broadband Ge modulator-detector co-integration over an optical bandwidth of 100 nm from 1,520 to 1,630 nm across C- and L-bands, labelled by the blue region. c Operational wavelength coverage (solid bars, from measurement; shadowed bars, from calculation) of co-integrated strained (tensile: 600 MPa, compressive: 1 GPa) Ge-based modulator arrays (mesa widths from 0.4 to 4.0 μm) and waveguide-integrated photodetectors (mesa width: 0.4 μm) as a function of Si composition. Respective fiber-optic communication bands are labelled at the top.

Supplementary Files

This is a list of supplementary files associated with this preprint. Click to download.

- [SupplementaryInformationfinal.docx](#)